AN EVALUATION OF RANS TURBULENCE CLOSURE MODELS FOR SPILLING BREAKERS

S.A. Brown[1], V. Magar[2], D.M. Greaves[1] and D.C. Conley[1]

Breaking waves generate turbulence which, along with the bottom stress, undertow, and other mean currents, is capable of suspending and transporting large quantities of sediment. In the present work, open source computational fluid dynamics software is utilised to evaluate four different turbulence models for the application of spilling breakers in the surf zone. The turbulence models are compared against both existing laboratory data and previous numerical models for surface elevation, velocity and turbulent kinetic energy profiles. The results imply that the different models vary in performance for each of these properties and that for incompressible, multiphase flows, it is important to include density explicitly in the turbulence transport equations. Overall, it was found that, out of the models considered, the best one for spilling breakers is the nonlinear $k-\epsilon$ model.

Keywords: spilling breakers; turbulence models; computational fluid dynamics; OpenFOAM; surf zone

INTRODUCTION

Suspended sediment transport is most influential in environments where large quantities of fine sands are found. Suspended sediments have a great impact on physical and biological processes, for instance, coastal erosion and light penetration through the water column. Hence, it is essential to be able to predict suspended sediment concentrations and sediment transport rates with good accuracy. As a consequence, substantial research effort has been put into understanding the processes behind suspended sediment dynamics.

A significant consideration when predicting suspended sediment concentrations in the surf and swash zones, is the effect of breaking waves. In the surf zone, breaking waves generate turbulence to levels capable of suspending and transporting large quantities of sediment. Such breaker-induced turbulence is influenced mainly by the Iribarren number, ξ_0, (Battjes (1974); Iribarren and Nogales (1949)), the breaker's steepness and the beach. The value of the Iribarren number indicates the type of breaker, defined as spilling ($\xi_0 < 0.5$), plunging ($0.5 < \xi_0 < 3.3$) or collapsing ($3.3 < \xi_0$). Turbulence generated by spilling breakers on a sloping beach has been investigated both experimentally (Ting and Kirby (1994, 1996)) and numerically (Lin and Liu (1998); Bradford (2000); Christensen et al. (2000); Xie (2013)), with varying results. For example, the numerical simulations generally overestimate the levels of turbulent kinetic energy (TKE) generated by the breakers.

In this work, the effect of turbulence generated by spilling breakers on suspended sediment dynamics is investigated, using the open source computational fluid dynamics (CFD) code, OpenFOAM (OpenFOAM (2014)) based on the Reynolds Averaged Navier-Stokes (RANS) equations. Here, waves are generated using the module waves2Foam, a wave generation toolbox developed by Jacobsen et al. (2012). The current model is tested against previous surf zone turbulence results, both numerical and experimental.

The paper is organised as follows. First, an overview of the turbulence models is given. Then, the numerical setup is presented, followed by a comparison of the turbulence models against laboratory and numerical data. Finally, the conclusions are drawn.

TURBULENCE MODELS

This work focuses on four RANS-type, turbulent eddy viscosity models, that fall into two groups. Both groups solve for the turbulent kinetic energy (TKE), k, and either the turbulence dissipation rate, ϵ, ($k-\epsilon$ models) or a characteristic frequency, ω, associated with the turbulence ($k-\omega$ models). This section describes the different models used and the advantages and disadvantages of each.

$k-\epsilon$ models are a commonly used method for turbulence closure. Hence, the weaknesses of the standard $k-\epsilon$ model are generally well known. One of these weaknesses is that the transport equation for ϵ becomes singular near the wall, so, in order to model the viscous sublayer accurately, it is necessary to introduce damping at the wall. Furthermore, fully developed, isotropic turbulence is assumed, so the model generally under-performs under transitional turbulence or adverse pressure gradients (Versteeg and Malalasekera (1995); Wilcox (2006)). The renormalised group (RNG) $k-\epsilon$ and a nonlinear $k-\epsilon$ model aim to address weaknesses of the standard $k-\epsilon$ model. The RNG $k-\epsilon$ model, originally developed using an additional

[1]School of Marine Science and Engineering, Plymouth University, United Kingdom
[2]Department of Physical Oceanography, CICESE, Ensenada, Mexico

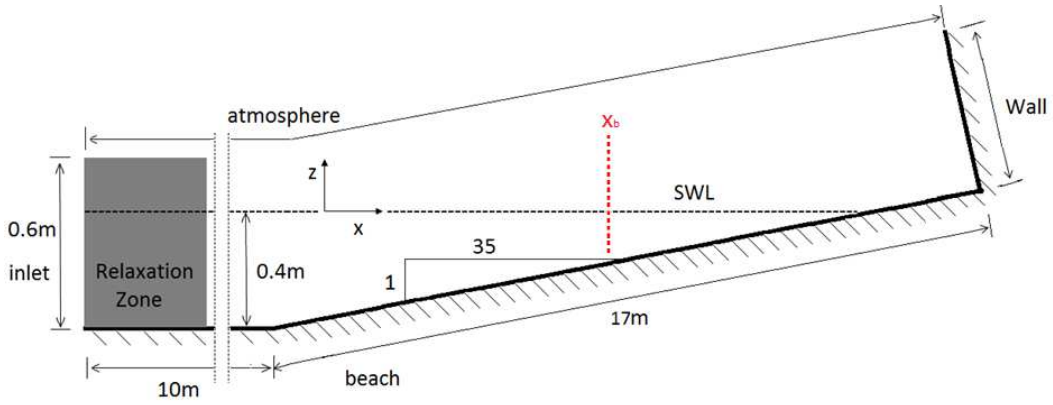

Figure 1: Diagram of the computational domain (not to scale) and the boundary names used.

expansion parameter by Yakhot et al. (1992), has been shown to perform better than the standard model in transitional flows (Versteeg and Malalasekera (1995)). However, the additional expansion parameter causes the model to be sensitive to the magnitude of the strain rate. Furthermore, the model is based upon the assumption of isotropy, which is not valid for all flows.

In this study, the validity of the isotropic assumption is considered by using a nonlinear $k-\epsilon$ model developed by Shih et al. (1996), which accounts for anisotropic effects by introducing a nonlinear Reynolds stress term into the standard $k-\epsilon$ model. Shih et al. (1996) showed the nonlinear $k-\epsilon$ model performs better than the standard $k-\epsilon$ model under strong adverse pressure gradients, as well as for separated and swirling flows.

Another model being evaluated is the $k-\omega$ model (Wilcox (2006)). It offers improved near wall treatment, removing the necessity for wall damping. It has also been shown to give more accurate predictions, than the standard $k-\epsilon$ model, in cases of adverse pressure gradients (Wilcox (2006)). However, it can be sensitive to inlet free stream boundary conditions and still relies on the isotropic turbulence assumption. The final model being considered is the $k-\omega$ shear stress transport (SST) model, developed by Menter (1994) and is a blend of both the $k-\omega$ and $k-\epsilon$ model. It aims to address the sensitivity to the free stream value of ω, whilst keeping the improved near wall treatment. To achieve this, a blending function is utilised, which applies the $k-\omega$ model for near wall treatment and the $k-\epsilon$ in the free stream. However, not all of the problems with $k-\omega$ and $k-\epsilon$ models are fixed by this method, since it also assumes that turbulence is isotropic.

NUMERICAL MODEL

The four turbulence models discussed above are tested for 2D spilling breakers propagating perpendicularly to the shore. The free surface is tracked using a two-phase volume of fluid (VOF) technique, solved together with the incompressible RANS equations for the flow field. The coordinate system (x, y, z) is taken such that x corresponds to the cross-shore direction, with the waves being generated on the left at the inlet boundary and propagating towards a beach located on the right of the domain (see Figure 1). y and z are the long-shore and vertical coordinates, respectively. Waves are generated at the inlet by setting a time-dependent boundary condition for the velocity and the free surface, both based on analytical solutions of the wave equations. A relaxation zone at the inlet permits absorption of wave reflections at the boundary. A Courant number of 0.2 is chosen, for numerical stability. It was found that this condition is necessary for both explicit and implicit schemes.

Computational Domain & Boundary Conditions

The computational domain is setup to be consistent with the laboratory experiments of Ting and Kirby (1994) and is shown in Figure 1. There is a sloping beach of gradient 1/35, the water depth, h, is 0.4m and the origin is located at the still water line, 0.7m shoreward of the start of the slope, where h=0.38m (see Figure 1). Approximately 320000 cells are used to discretise the domain, which is only one cell thick in the y direction. In the x and z directions the cells have an aspect ratio of 1 where possible, i.e. $\Delta x = \Delta z$. This was shown to improve the breaking point and height of the wave by Jacobsen et al. (2012), who suggested that

this was due to larger VOF flux in cells of aspect ratio greater than one. The cell size in the internal domain is set to 0.01m but, after an initial study, it was found that refinement around the free surface significantly improved the results for the current model. Therefore, further refinement is applied in the x and z directions so that the discretisation is 0.005m in this region. At the beach boundary six layers of thinner cells (in the z direction) have been used, with each layer away from the boundary being twice the size of the last.

Waves of period $T = 2$s and height $H = 0.125$m are generated using stream function wave theory at the inlet boundary condition. A relaxation zone of approximately one wavelength, L, is applied at the inlet boundary. This has been shown to allow simulation, and therefore averaging, over a large number of waves (Jacobsen et al. (2012)). The model is run for fifty wavelengths, with the final twenty waves averaged and used for the results in this study. Data is collected relative to the breaking point of the wave at the probe locations considered by Ting and Kirby (1994).

The beach and Wall boundaries are considered as solid walls and therefore no-slip conditions have been applied along with zero gradient conditions for pressure and VOF. The atmosphere also uses a Neumann boundary condition for the VOF but the boundary condition for the velocity varies according to the near boundary flux; using a zero gradient condition for outflow and the internal cell value of the normal component to the patch face for the inflow. The atmosphere boundary condition for pressure is defined as the total pressure

$$p = p_0 + \frac{1}{2}|\mathbf{u}|^2 \tag{1}$$

where p_0 is the user defined reference value, and $\mathbf{u}$ is the velocity. For this case p_0 is set to zero since the solver uses the difference between total pressure and hydrostatic pressure. The initial conditions are set to the solution after running the model without a turbulence model turned on for fifty wave periods.

Wall functions are applied at the beach boundary. The wall functions switch between low Reynolds number (LRN) and high Reynolds number (HRN) flows, depending on whether the near wall cell centre lies in the log or laminar sublayer. This is evaluated through the dimensionless wall distance

$$z^+ = \frac{\Delta z_w u_*}{\nu} = \frac{\Delta z_w \sqrt[4]{C_\mu}\sqrt{k}}{\nu}, \tag{2}$$

where z_w is the distance from the near wall cell centre to the wall. Comparing z^+ to the threshold value at the edge of the laminar sublayer, z^+_{lam}, gives an indication as to the region in which the near wall centre lies. The value of z^+_{lam} is obtained by solving

$$z^+_{lam} = \frac{\log(z^+_{lam}E)}{\kappa} \tag{3}$$

where E is an integration constant associated with the surface roughness and κ is the von Kármán constant. If $z^+ > z^+_{lam}$, the cell centre is assumed to be in the log layer and a HRN wall function is used. Conversely, if $z_+ \leq z^+_{lam}$ then the cell centre is assumed to be below the log layer and therefore a LRN wall function is used. Neumann boundary conditions are applied for each of the turbulent variables at the Wall boundary. At all the other boundaries the turbulent boundary conditions must be chosen carefully since, although TKE should not exist at the walls, Lin and Liu (1998) note that the transport equations become singular if $k = 0$, making it necessary to 'seed' a small quantity of TKE. Following Lin and Liu (1998), the TKE at the inlet is calculated as

$$k = \frac{1}{2}(c_p^2 I) \tag{4}$$

where I and $c_p = L/T$ are the turbulence intensity and phase speed of the wave, respectively. The ϵ or ω value is then adjusted so that the eddy viscosity is a fraction, λ, of the kinematic viscosity, i.e. $\nu_t = \lambda\nu$. Following Lin and Liu (1998), I and λ are chosen as 0.0025 and 0.1, respectively, in this study. The initial conditions are set to the value specified at the inlet.

Implementation of Turbulence Models

In this section, the transport equations for each of the turbulence models under consideration are discussed with particular emphasis on how they are implemented in OpenFOAM (version 2.1.1). The general form of the equations is such that

rate of change + transport by convection = production − dissipation + transport by diffusion

Each model has two transport equations, one for TKE and another for either ϵ or ω and the values obtained from solving these equations are used to compute the eddy viscosity. It is worth noting that all of the incompressible solvers implemented in OpenFOAM, including those for multiphase flows, do not include density explicitly but instead model the kinematic eddy viscosity, ν_t rather than the dynamic form, μ_t.

The $k-\omega$ model (Wilcox (1988)) solves the following transport equations for k and ω,

$$\frac{\partial k}{\partial t} + \nabla \cdot (\mathbf{u}k) = P_k - C_\mu \omega k + \nabla \cdot [(\nu + \sigma_k \nu_t)\nabla k], \tag{5}$$

$$\frac{\partial \omega}{\partial t} + \nabla \cdot (\mathbf{u}\omega) = \frac{\gamma \omega}{k} P_k - \beta \omega^2 + \nabla \cdot [(\nu + \sigma_\omega \nu_t)\nabla \omega], \tag{6}$$

with $\sigma_k = \sigma_\omega = 0.5$, $C_\mu = 0.09$, $\beta = 0.072$ and $\gamma = 0.52$. The production term is defined as $P_k = \nu_t |S|^2$, defining S in terms of the mean rate of strain of the flow, $\mathbf{S}$, as

$$S = \sqrt{2\mathbf{S}:\mathbf{S}}, \qquad \mathbf{S} = \frac{1}{2}\left(\nabla \mathbf{u} + (\nabla \mathbf{u})^T\right), \tag{7}$$

where **:** is the double inner product. The values of k and ω are obtained by solving equations (5) and (6), and are then used to compute the eddy viscosity, $\nu_t = k/\omega$.

The $k-\omega$ SST model, originally developed by Menter (1994), solves the equations

$$\frac{\partial k}{\partial t} + \nabla \cdot (\mathbf{u}k) = \min(P_k, c_1 C_\mu k \omega) - C_\mu \omega k + \nabla \cdot [(\nu + \sigma_k \nu_t)\nabla k] \tag{8}$$

$$\frac{\partial \omega}{\partial t} + \nabla \cdot (\mathbf{u}\omega) = \frac{\gamma P_k}{\nu_t} - \beta \omega^2 + \nabla \cdot [(\nu + \sigma_\omega \nu_t)\nabla \omega] + 2(1 - F_1)\frac{\sigma_{\omega 2}}{\omega}\nabla k \cdot \nabla \omega \tag{9}$$

where P_k is the same as in the $k-\omega$ model. The coefficients σ_k, σ_ω, β and γ are a blend of an inner constant (subscript 1) and an outer constant (subscript 2), blended according to

$$\phi = F_1 \phi_1 + (1 - F_1)\phi_2. \tag{10}$$

The function F_1 used in the blending function is described by

$$F_1 = \tanh(\Gamma_1^4), \qquad \Gamma_1 = \min\left(\min\left(\left[\max\left\{\frac{\sqrt{k}}{C_\mu \omega \Delta z_w}, \frac{500\nu}{\Delta z_w^2 \omega}\right\}\right], \frac{4\sigma_{\omega 2} k}{CD_{k\omega}\Delta z_w^2}\right), 10\right) \tag{11}$$

where

$$CD_{k\omega} = \max\left\{\frac{2\sigma_{\omega 2}}{\omega}\nabla k \cdot \nabla \omega, 10^{-10}\right\} \tag{12}$$

and Δz_w is the distance from the field point to the nearest wall. The values for the inner and outer constants are given in Table 1. The eddy viscosity is then calculated by

$$\nu_t = \frac{a_1 k}{\max\{a_1 \omega, b_1 F_2 S\}} \tag{13}$$

where

$$F_2 = \tanh(\Gamma_2^2), \qquad \Gamma_2 = \min\left(\max\left\{\frac{2\sqrt{k}}{\omega \Delta z_w}, \frac{500\nu}{\Delta z_w^2 \omega}\right\}, 100\right), \tag{14}$$

Table 1. Default values for the inner and outer constants in the $k-\omega$ SST model.

σ_{k1}	σ_{k2}	$\sigma_{\omega 1}$	$\sigma_{\omega 2}$	β_1	β_2	C_μ	γ_1	γ_2	a_1	b_1	c_1
0.85034	1.0	0.5	0.85616	0.075	0.0828	0.09	0.5532	0.4403	0.31	1.0	10.0

The RNG $k-\epsilon$ model solves two equations for k and ϵ defined as

$$\frac{\partial k}{\partial t} + \nabla \cdot (\mathbf{u}k) = P_k - \epsilon + \nabla \cdot [(\nu + \sigma_k \nu_t)\nabla k], \tag{15}$$

$$\frac{\partial \epsilon}{\partial t} + \nabla \cdot (\mathbf{u}\epsilon) = \frac{C^*_{1\epsilon} P_k \epsilon}{k} - \frac{C_{2\epsilon}\epsilon^2}{k} + \nabla \cdot [(\nu + \sigma_\epsilon \nu_t)\nabla \epsilon], \tag{16}$$

The coefficient $C^*_{1\epsilon}$ differs between the standard $k-\epsilon$ and RNG $k-\epsilon$ models (see Speziale and Thangam (1992)). In the former it is just $C_{1\epsilon}$ and in the latter is derived as

$$C^*_{1\epsilon} = C_{1\epsilon} - \frac{\eta(1-\eta/\eta_0)}{1+\beta\eta^3}. \tag{17}$$

In equation (17), η is the additional expansion parameter used in the derivation by Yakhot et al. (1992), defined as the time scale ratio of the turbulent to the mean strain rate, $\eta = Sk/\epsilon$. The eddy viscosity is computed by

$$\nu_t = C_\mu \frac{k^2}{\epsilon} \tag{18}$$

All of the model coefficients, except β which is obtained through experiments, are obtained through the derivation of the RNG $k-\epsilon$ model and are set to $C_\mu = 0.0845$, $\sigma_k = \sigma_\epsilon = 1.39$, $C_{1\epsilon} = 1.42$, $C_{2\epsilon} = 1.68$, $\eta_0 = 4.38$ and $\beta = 0.012$.

Nonlinear (NL) $k-\epsilon$ models are an alternative to Reynolds stress closure models. In this work, a model developed by Shih et al. (1996) is used, which relates the mean strain rate of the flow to the Reynolds stress tensor through the algebraic nonlinear Reynolds stress model. The model adjusts the Reynolds stress, $\boldsymbol{\tau}$, by adding a nonlinear stress term $\boldsymbol{\tau_{NL}}$, defined as

$$\boldsymbol{\tau_{NL}} = \frac{1}{2}(\boldsymbol{\chi} + \boldsymbol{\chi}^T) \tag{19}$$

$$\boldsymbol{\chi} = \frac{k^3}{(A_2+\eta^3)\epsilon^2}\Big(C_{\tau 1}[\nabla\mathbf{u}\cdot\nabla\mathbf{u} + (\nabla\mathbf{u}\cdot\nabla\mathbf{u})^T] + C_{\tau 2}[\nabla\mathbf{u}\cdot(\nabla\mathbf{u})^T] + C_{\tau 3}[(\nabla\mathbf{u})^T\cdot\nabla\mathbf{u}]\Big), \tag{20}$$

where $C_{\tau 1}$, $C_{\tau 2}$, $C_{\tau 3}$ and A_2 are constants. The parameter η is defined the same as in the RNG $k-\epsilon$ model, with k and ϵ being calculated using equations (15) and (16), with different values for the coefficients ($C^*_{1\epsilon} = 1.44$, $C_{2\epsilon} = 1.92$, $\sigma_\epsilon = 0.77$, $\sigma_k = 1$). The nonlinear stress term is also used in the production term, P_k, which is defined as

$$P_k = \rho(\nu_t \mathbf{S}{:}\nabla\mathbf{u} - \boldsymbol{\tau_{NL}}{:}\nabla\mathbf{u}) \tag{21}$$

The eddy viscosity is obtained through the same relationship as in the RNG $k-\epsilon$ (equation (18)) except that the value of C_μ depends upon the values of ξ and η,

$$C_\mu = \frac{2}{3(A_1 + \eta + \alpha_\xi \xi)}, \tag{22}$$

where α_ξ and A_1 are constants and $\xi = \Omega k/\epsilon$ is an additional parameter, where Ω, defined in terms of the mean rate of rotation, $\boldsymbol{\Omega}$, is

$$\Omega = \sqrt{2\boldsymbol{\Omega}{:}\boldsymbol{\Omega}}, \qquad \boldsymbol{\Omega} = \frac{1}{2}\Big(\nabla\mathbf{u} - (\nabla\mathbf{u})^T\Big), \tag{23}$$

COMPARISON WITH LABORATORY DATA

Tests are first performed with density not explicitly considered in the turbulence model transport equations, and is only taken into account through the kinematic eddy viscosity, ν_t. Comparisons between the model predictions and observations by Ting and Kirby (1994), under the same wave conditions, for the maximum, mean and minimum surface elevation (Figure 2), for the time averaged velocity (Figure 3), and for the mean turbulent kinetic energy profiles (Figure 4), are presented.

Figure 2 shows the surface elevations $\eta_{max} - \overline{\eta}$, $\overline{\eta}$ and $\eta_{min} - \overline{\eta}$ as a function of horizontal distance, x, along the numerical wave flume. Here η_{max} and η_{min} are the maximum and minimum phase averaged

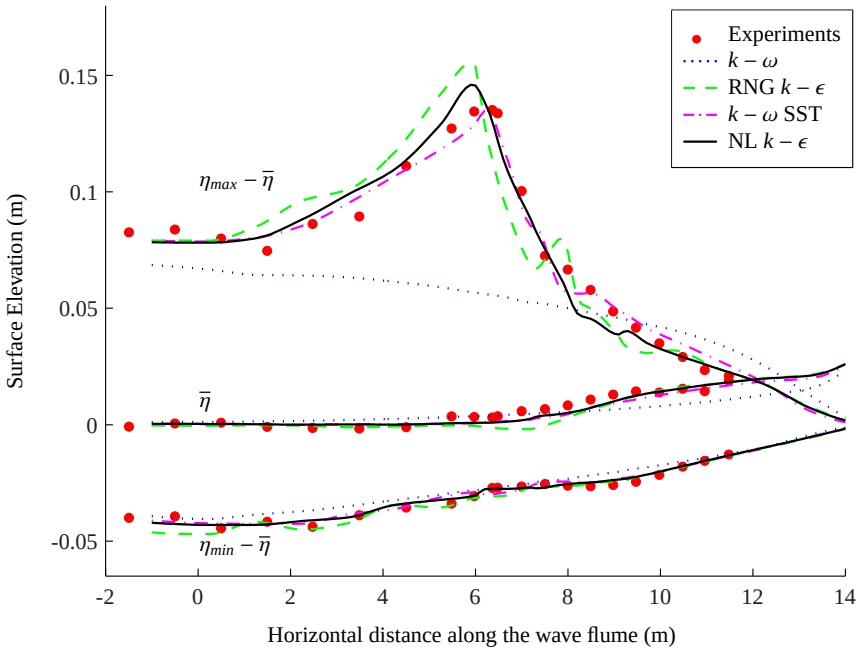

Figure 2: Comparison of the maximum, minimum and mean phase-averaged surface elevation against x coordinate. Each line represents a different turbulence closure model and the dots are from the experimental data collected by Ting and Kirby (1994).

surface elevation and $\overline{\eta}$ is the mean surface elevation. The red dots represent the experimental data gathered by Ting and Kirby (1994), whereas the lines indicate the predictions by each of the turbulence models considered. The plot implies that all of the turbulence models perform reasonably well with respect to the experimental data for mean and minimum values. However, the $k-\omega$ model's prediction of the maximum breaker height is very poor compared to the other three turbulence models. Hence, this model will not be tested further under the conditions and model setup discussed in this section. In contrast, although the RNG and nonlinear $k-\epsilon$ models overestimate the breaking height and predict breaking earlier along the flume than expected, they still give reasonable results. Of all the models considered, the $k-\omega$ SST model is the one that performs best for the water elevation predictions.

Figure 3 shows the variation of the time averaged horizontal velocity, $\overline{u}$ (ms^{-1}) profiles with dimensionless depth, $(z-\overline{\eta})/h$. Once again, the red dots represent the experimental data presented by Ting and Kirby (1994), and the lines each of the turbulence models considered. Each subplot shows a different sampling location relative to the breaking point, one corresponding to pre-breaking (5.945m in Ting and Kirby (1994)), and three post-breaking (7.275, 8.495 and 9.725m in Ting and Kirby (1994)). All three remaining models fail to capture the pre-breaking profile (plot a) since they predict a moderate undertow, which was not observed in the experiments. However, as the undertow begins to develop in the experiments (plot b), the accuracy of the models begin to improve, with the nonlinear $k-\epsilon$ model giving the best results. Further down the flume (plots c and d), where the undertow is strongest in the experiments, both the nonlinear $k-\epsilon$ and $k-\omega$ SST models perform well but the RNG $k-\epsilon$ appears to over predict the undertow.

Figure 4 shows the changes of the mean turbulent kinetic energy, $\overline{k}$ (m^{2}s^{-2}), with dimensionless depth. As before, the red dots represent the experimental data collected by Ting and Kirby (1994) and the lines indicate the predictions by each of the different turbulence models considered. Similar to the velocity plots in Figure 3, each subplot represents a different sampling location relative to the breaking point. All five locations considered are after breaking has occurred and correspond to locations 7.275, 7.885, 8.495, 9.11 and 9.725m in Ting and Kirby (1994). Despite the $k-\omega$ SST model performing well for both surface elevation and velocity profiles, the predictions of TKE at all five locations are much larger than the experimental data suggests. The RNG $k-\epsilon$ model gives good predictions in plot a, but becomes progressively worse down the flume. Although the nonlinear $k-\epsilon$ model over predicts the TKE in every plot, it is probably the

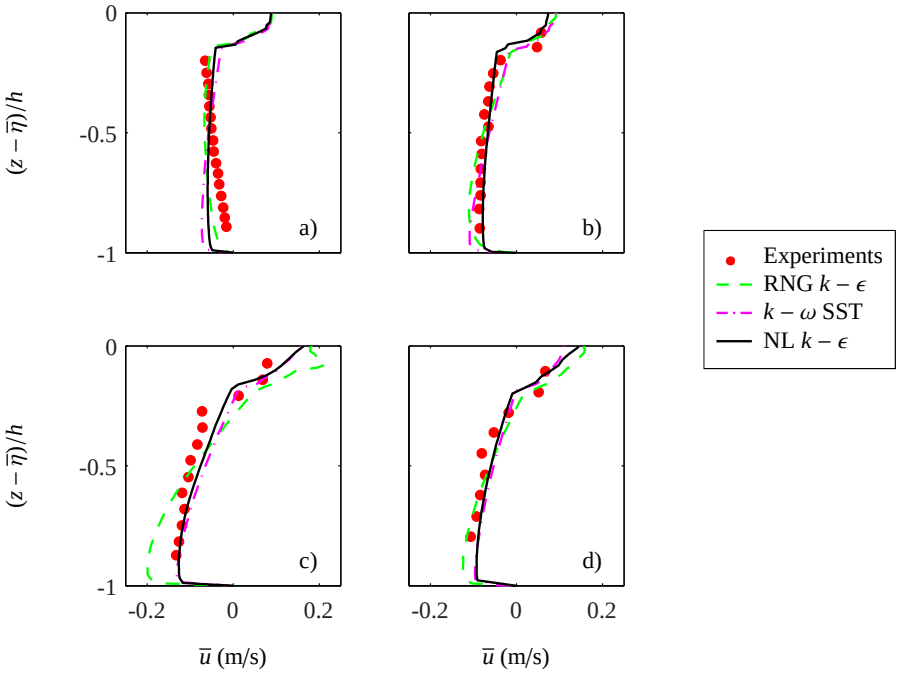

Figure 3: Comparison of time averaged velocity profiles with depth at sampling locations $x - x_b$ = a) -0.455, b) 0.875, c) 2.095 and d) 3.325m. Each line represents a different turbulence closure model and the dots indicate the experimental data gathered by Ting and Kirby (1994).

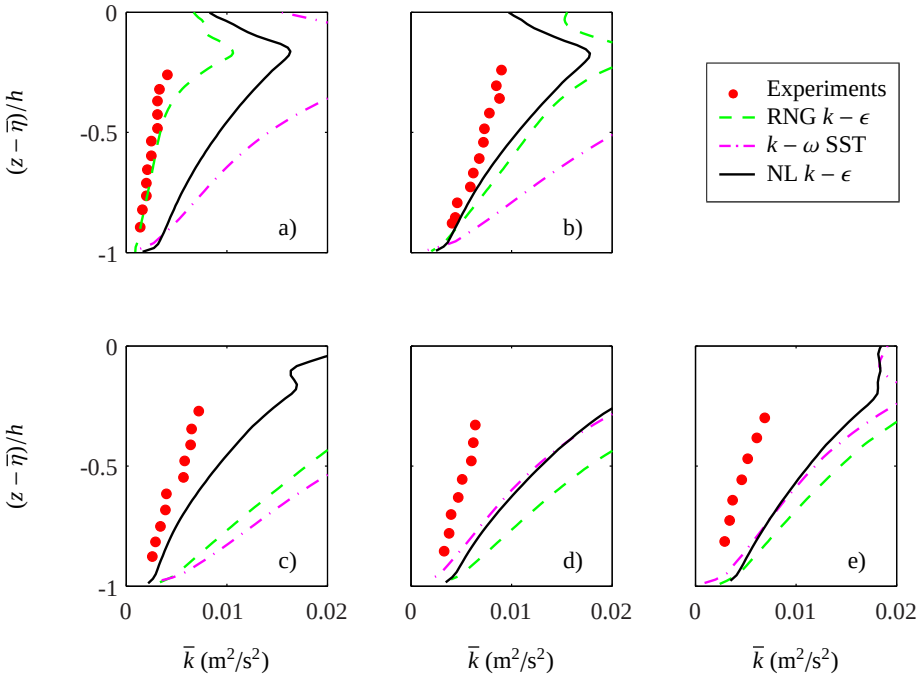

Figure 4: Comparison of time averaged TKE profiles with depth at sampling locations $x - x_b$ = a) 0.875, b) 1.485, c) 2.095, d) 2.71 and e) 3.325m. Each line represents a different turbulence closure model and the dots indicate the experimental data presented by Ting and Kirby (1994).

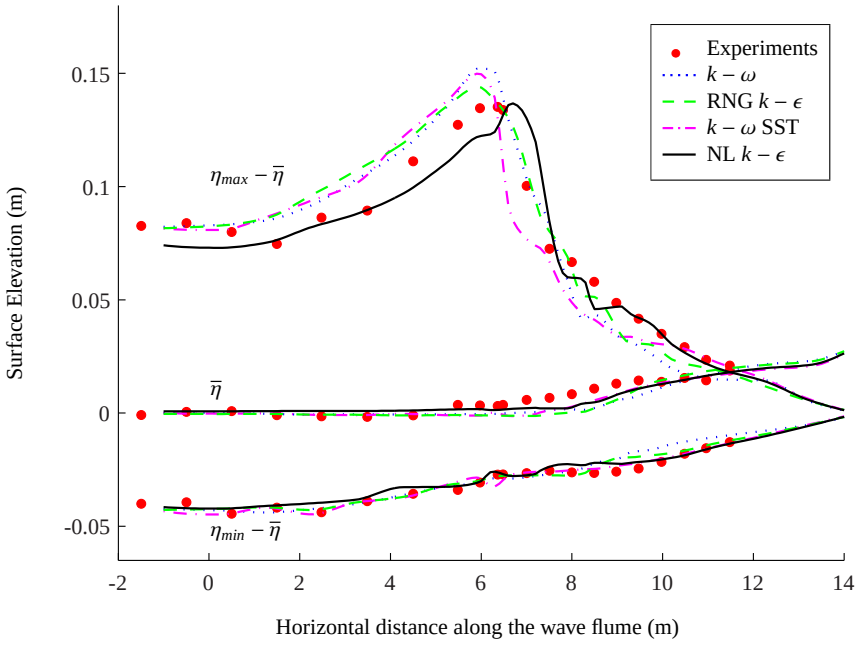

Figure 5: Comparison of the maximum, minimum and mean phase-averaged surface elevation against x coordinate. Each line represents a different turbulence closure model (with density included explicitly) and the dots indicate the experimental data obtained by Ting and Kirby (1994).

better of the three models since, with the exception of location a, it gives smaller predictions than the RNG $k-\epsilon$ model at all of the other sampling points. Generally, the turbulence models perform much better in the bottom half of the water column and struggle to predict levels closer to the free surface.

It is worth noting that the omitted $k-\omega$ model, predicts TKE to be ten times larger than observed in the experiments. It is believed that this significant over prediction of TKE is responsible for the excessive damping observed in the free surface since it corresponds to larger contributions to the Reynolds stress, which is a negative contribution to the RANS equations and hence relates to more energy being removed from the mean flow.

Explicit inclusion of density in the turbulence models

In an attempt to improve the predictions of TKE, a slight modification has been made, following Jacobsen (2011), to the implementation of the OpenFOAM turbulence models. In OpenFOAM all incompressible turbulence models, both for single and multiple phases, take a form where the density is only implicitly represented in the transport equations through the kinematic eddy viscosity, $\nu_t = \mu_t/\rho$. This is fine for single phase flows. However, in order to be able to take ρ outside of a derivative, it must be assumed that it is constant. In a VOF scheme, the two phases are modelled as a fluid with a variable density. Hence, around the free surface the assumption of constant density will not hold since it will vary between the value for air and the value of water. As noted by Jacobsen (2011), this causes excessive diffusion of turbulence over the free surface interface and since $\nu_{t,water} \ll \nu_{t,air}$, the wave will be damped. Therefore, the transport equations for each turbulence model are altered to include density explicitly, e.g. equation 5 becomes

$$\frac{\partial \rho k}{\partial t} + \nabla \cdot (\rho \mathbf{u} k) = \rho P_k - \rho C_\mu \omega k + \nabla \cdot [\rho(\nu + \sigma_k \nu_t)\nabla k] \tag{24}$$

Each turbulence model has then been run again with the same setup as in the previous section. Figure 5 shows the phase averaged surface elevations $\eta_{max} - \overline{\eta}$, $\overline{\eta}$ and $\eta_{min} - \overline{\eta}$ as a function of horizontal distance, x, along the numerical wave flume, for each of the turbulence models with density explicitly included. The red dots represent the experimental data gathered by Ting and Kirby (1994) and the lines indicate the results of each of the different turbulence models considered. Similar to the results without density included (Figure 2), there seems to be very little difference between any of the turbulence closure models in terms

Table 2. Summary of the information at breaking for each turbulence model. x_b is the breaking point, d_b, h_b are the depth from the SWL ($x = 0$) and MWL ($x = \xi_b$), respectively, and H_b is the wave height at breaking.

	$k-\omega$		RNG $k-\epsilon$		$k-\omega$ SST		NL $k-\epsilon$		Ting (1994)
	w/o ρ	w. ρ	w/o ρ	w. ρ	w/o ρ	w. ρ	w/o ρ	w. ρ	Exp. Data
x_b (m)	-	6.2	5.9	5.9	6.2	5.9	5.9	6.7	6.4
d_b (m)	-	0.2029	0.2114	0.2114	0.2029	0.2114	0.2114	0.1886	0.196
ξ_b (m)	-	-0.0004	-0.0004	-0.001	0.0011	-0.0011	0.0008	0.0019	0.0033
h_b (m)	-	0.2025	0.211	0.2104	0.204	0.2103	0.2122	0.1905	0.1993
H_b (m)	-	0.1807	0.1876	0.1740	0.1647	0.1783	0.1769	0.1645	0.1621

of the mean and minimum surface elevation. However, by comparing to Figure 2, very obvious differences occur in the maximum surface elevation profile, with the inclusion of density significantly increasing the performance of the $k-\omega$ turbulence model. The maximum value now performs much better, with reasonable agreement with the experimental data, although, similar to the RNG $k-\epsilon$ and $k-\omega$ SST turbulence models, the maximum surface elevation seems to be slightly overestimated prior to breaking, with the breaking point also occurring slightly earlier than expected. On the other hand, the nonlinear $k-\epsilon$ model breaks slightly further down the flume than shown in the experiments. The breaking points of each of the models, both with (w. ρ) and without (w/o ρ) density, have been summarised in Table 2, along with the water depths and wave height at breaking. Overall it appears that the inclusion of density has improved the maximum surface elevation profile near the breaking point for both the RNG and nonlinear $k-\epsilon$ models but has caused the $k-\omega$ SST models accuracy to drop.

Figure 6 shows the mean horizontal velocity, $\overline{u}$, profiles with dimensionless depth. As before the red dots represent the experimental data presented by Ting and Kirby (1994), and the lines each of the turbulence models, with density explicitly included. Once again, each subplot shows a different sampling location relative to the breaking point, location a is pre-breaking (5.945m in Ting and Kirby (1994)), and locations b-d are post-breaking (7.275, 8.495 and 9.725m in Ting and Kirby (1994)). Comparing with Figure 3, it is clear that modifying the equations has caused the RNG $k-\epsilon$ model to capture the negative gradient of velocity with depth shown in subplot a, which the other three models still can not predict. However, this model, along with the $k-\omega$ SST and $k-\omega$ models, does not capture the profile after breaking, with a significantly larger undertow being predicted at locations c and d than was found in the experiments by Ting and Kirby (1994). Conversely, the nonlinear $k-\epsilon$ model does not capture the pre-breaking profile but captures the undertow well after breaking.

Figure 7 shows the time averaged TKE, $\overline{k}$, profiles with dimensionless depth. Once again, the red dots represent the experimental data collected by Ting and Kirby (1994) and the lines indicate the predictions by each of the turbulence models, with density explicitly included. Each subplot represents a different sampling location relative to the breaking point. All five locations are placed after breaking has occurred and correspond to locations 7.275, 7.885, 8.495, 9.11 and 9.725m in Ting and Kirby (1994). When compared to the results before density was included (Figure 4), it is clear that the magnitude of the TKE is generally smaller over the five plots for each of the turbulence closure models considered in this work. The $k-\omega$ model shows remarkable improvement; before the modification the TKE was around ten times larger than the experimental data but it now performs well and is probably the most accurate of the four models overall. It is believed that this improvement in TKE profiles is the reason for the significant improvement in surface elevation since less damping occurs. The $k-\omega$ SST model has also improved. Instead of over-predicting the TKE at every location, good accuracy is obtained at the sampling location closest to the breaking point (subplots a) but progressively over estimates the magnitude further down the flume. The RNG $k-\epsilon$ model follows a similar pattern, it begins by under-estimating the TKE in subplots a and b and then over-estimates in subplots d and e. Finally, the nonlinear $k-\epsilon$ model gives similar results to the $k-\omega$ model, except in subplots a and c where it significantly over predicts the magnitude of the TKE.

Discussion

Up to this point all the analysis has been made visually but in this section, the strengths and weaknesses of each turbulence model are assessed by considering the normalised root mean square error (NRMSE). Table 3 shows the NRMSE for each turbulence model, both with (w. ρ) and without (w/o ρ) density

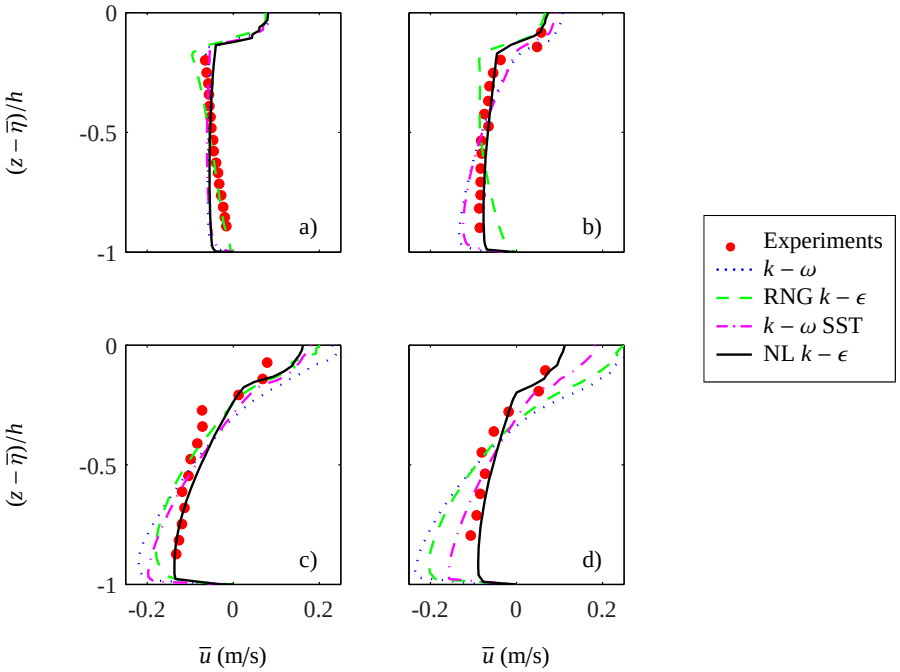

Figure 6: Comparison of time averaged velocity profiles with depth at sampling locations $x - x_b$ = a) -0.455, b) 0.875, c) 2.095 and d) 3.325m. Each line represents a different turbulence closure model (with density included explicitly) and the dots indicate the experimental data reported by Ting and Kirby (1994).

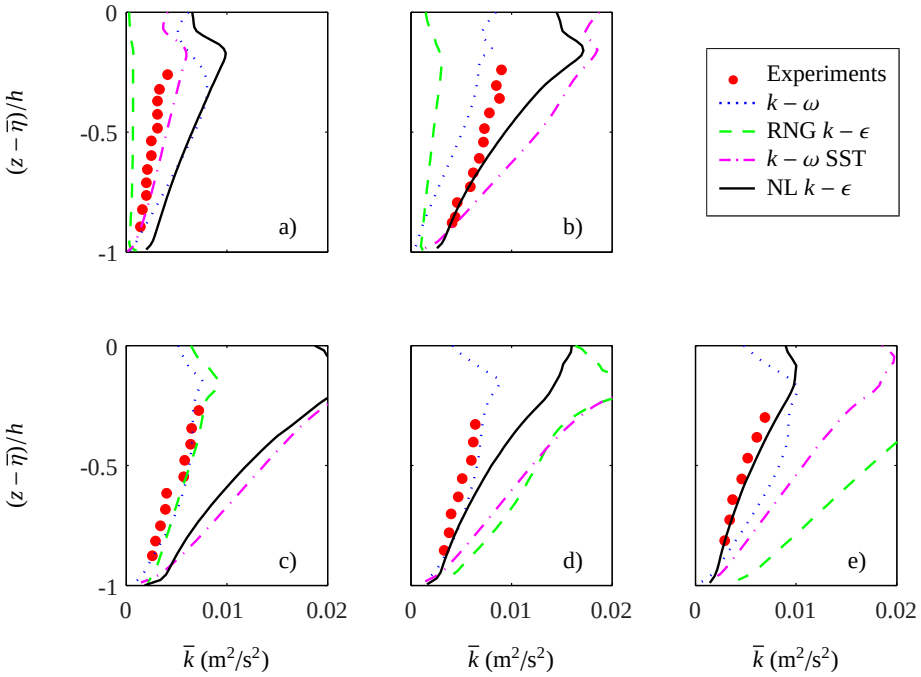

Figure 7: Comparison of time averaged TKE profiles with depth at sampling locations $x - x_b$ = a) 0.875, b) 1.485, c) 2.095, d) 2.71 and e) 3.325m. Each line represents a different turbulence closure model (with density included explicitly) and the dots indicate the experimental data gathered by Ting and Kirby (1994).

Table 3. Normalised root mean square error (NRMSE) with respect to the experimental data gathered by Ting and Kirby (1994), for each turbulence closure model, both with (w. ρ) and without (w/o ρ) density included explicitly. The model with the lowest NRMSE is indicated by bold text in each case.

		$k-\omega$		$k-\omega$ SST		RNG $k-\epsilon$		NL $k-\epsilon$	
		w/o ρ	w. ρ	w/o ρ	w. ρ	w/o ρ	w. ρ	w/o ρ	w. ρ
η	Max	0.338	0.097	**0.046**	0.111	0.117	0.079	0.063	0.087
	Min	0.112	0.109	0.056	0.067	0.079	0.077	**0.048**	0.072
	MWL	0.197	0.201	0.119	0.168	0.173	0.217	**0.108**	0.146
	Mean	0.215	0.135	0.073	0.115	0.123	0.124	**0.073**	0.101
$\overline{u}$	plot a	0.548	0.441	0.640	0.429	0.408	**0.247**	0.460	0.401
	plot b	0.323	0.187	**0.120**	0.176	0.141	0.234	0.140	0.134
	plot c	0.339	0.308	0.146	0.213	0.274	0.179	**0.114**	0.142
	plot d	0.298	0.468	0.146	0.180	**0.131**	0.371	0.140	0.138
	Mean	0.377	0.351	0.263	0.250	0.239	0.258	0.214	**0.204**
$\overline{k}$	plot a	16.94	1.248	4.475	**0.420**	0.464	0.767	2.366	1.328
	plot b	8.381	**0.521**	2.762	0.985	1.036	0.975	0.754	0.555
	plot c	9.050	**0.171**	3.383	1.677	2.562	0.186	0.821	1.408
	plot d	12.65	**0.286**	2.141	1.901	3.684	2.049	2.201	0.784
	plot e	9.915	0.666	1.739	1.346	2.313	2.977	1.522	**0.182**
	Mean	11.39	**0.578**	2.900	1.266	2.012	1.391	1.533	0.851
Mean		4.924	**0.392**	1.314	0.639	0.949	0.697	0.728	0.448

included. Each plot considered in this work is listed with the turbulence closure model yielding the lowest value indicted through bold text in each case. The bold values are spread between the different turbulence models, indicating that all of the models predict different characteristics more accurately. For instance the RNG $k-\epsilon$ model has a much lower NRMSE than the other models for the velocity plot at location a, but the nonlinear $k-\epsilon$ model has the lowest at location c.

Furthermore, in order to evaluate how applicable the different turbulence closure models are, Table 3 shows the mean NRMSE for surface elevation, velocity and TKE profiles, as well as overall. The first thing to note is that for every turbulence model considered in this study, the largest and smallest errors occur in the TKE and surface elevation profiles, respectively. Furthermore, when modified to include density, every model has a significant reduction in TKE profile error, although it is still the largest contribution out of the properties considered. Only considering the models which include density, the results imply that the best turbulence model for surface elevation and velocity profiles in spilling breakers is the nonlinear $k-\epsilon$ model. However, the TKE profile is predicted best by the $k-\omega$ model, mainly due to the significantly larger predictions given by the nonlinear $k-\epsilon$ at locations c and d. This leads to the $k-\omega$ model having the smallest overall mean NRMSE. However, the nonlinear $k-\epsilon$ model is suggested as the best model overall for spilling breakers since, other than the two previously mentioned anomalies in the TKE, the model performs best. Therefore, this model has been chosen to carry forward and compare to the previous results of other authors who have done numerical investigations into spilling breakers.

COMPARISON WITH NUMERICAL INVESTIGATIONS

The nonlinear $k-\epsilon$ model, with density included explicitly, is compared to the results of three previous numerical studies; Bradford (2000) used the software FLOW-3D along with a RNG $k-\epsilon$ turbulence model, Jacobsen (2011) and Jacobsen et al. (2012), who also used OpenFOAM along with waves2Foam and a modified $k-\omega$ model and Xie (2013) who used a two phase code with a $k-\epsilon$ model. Along with including density, Jacobsen et al. (2012) modified the $k-\omega$ model, following Mayer and Madsen (2000), by changing the production term, P_k, in equation (5) to depend on the mean vorticity rather than the mean rate of strain of the flow. This was done in order to prevent any generation of TKE prior to breaking.

Figure 8 shows the surface elevations $\eta_{max}-\overline{\eta}$, $\overline{\eta}$ and $\eta_{min}-\overline{\eta}$ as a function of horizontal distance, x, along the numerical wave flume. The red dots represent the experimental data collected by Ting and Kirby (1994), whereas the lines indicate the predictions by each of the numerical models. There is very little

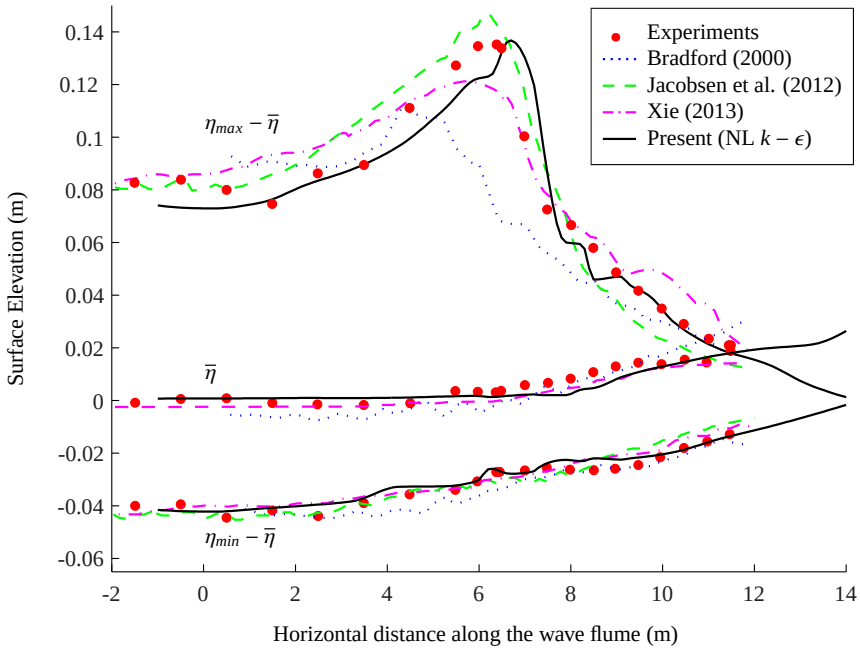

Figure 8: Comparison of the maximum, minimum and mean phase-averaged surface elevation against x coordinate. The current model as well as previous numerical models are indicated by the different lines and the dots represent the experimental data presented by Ting and Kirby (1994).

to choose between the models in terms of minimum and mean surface elevation. The maximum surface elevation at the breaking point is predicted best by the current model, since the models of Xie (2013) and Bradford (2000) underestimate this value whereas Jacobsen et al. (2012) is over predicted. However, the models of Jacobsen et al. (2012) and Xie (2013) capture the breaking point slightly better than the current model.

Figure 9 shows a comparison of the time averaged velocity profiles, $\overline{u}$, with dimensionless depth. Once again, the red dots represent the experimental data presented by Ting and Kirby (1994), and the lines are the results for each of the numerical models considered. Each subplot shows a different sampling location relative to the breaking point, one corresponding to pre-breaking (5.945m in Ting and Kirby (1994)), and three post-breaking (7.275, 8.495 and 9.725m in Ting and Kirby (1994)). The model of Jacobsen et al. (2012) captures the profile prior to breaking (subplot a) much more accurately than the nonlinear $k-\epsilon$ model from the current study, especially in the lower half of the water column. However, similar to the RNG $k-\epsilon$ considered earlier in this study, as the sampling location is moved down the flume, the undertow becomes over predicted by the model of Jacobsen et al. (2012), whereas the nonlinear $k-\epsilon$ model from the current work performs better in this region. The models of Xie (2013) and Bradford (2000) do not capture any of the profiles as well as the current model.

Figure 10 shows the time averaged TKE, $\overline{k}$, profiles with dimensionless depth. As before, the red dots represent the experimental data gathered by Ting and Kirby (1994) and the lines indicate the predictions by each of the numerical models. Similar to the TKE plots in Figure 4, each subplot represents a different sampling location relative to the breaking point. All five locations are placed after breaking has occurred and correspond to locations 7.275, 7.885, 8.495, 9.11 and 9.725m in Ting and Kirby (1994). The results imply that the model of Xie (2013) performs best, especially in subplots d and e. The current model follows a similar pattern to Xie (2013); at locations a and c there are large discrepancies between the experimental and current numerical model but good predictions occur in locations b and e. Bradford (2000) under predicts the profile at location a and overestimates at locations d and e. This is consistent with the RNG $k-\epsilon$ model considered in the present study. Jacobsen (2011) captures the TKE levels well at the earlier sampling locations but becomes progressively larger further away from the breaking point.

Table 4 shows the NRMSE for the different numerical models and all the plots shown in this section,

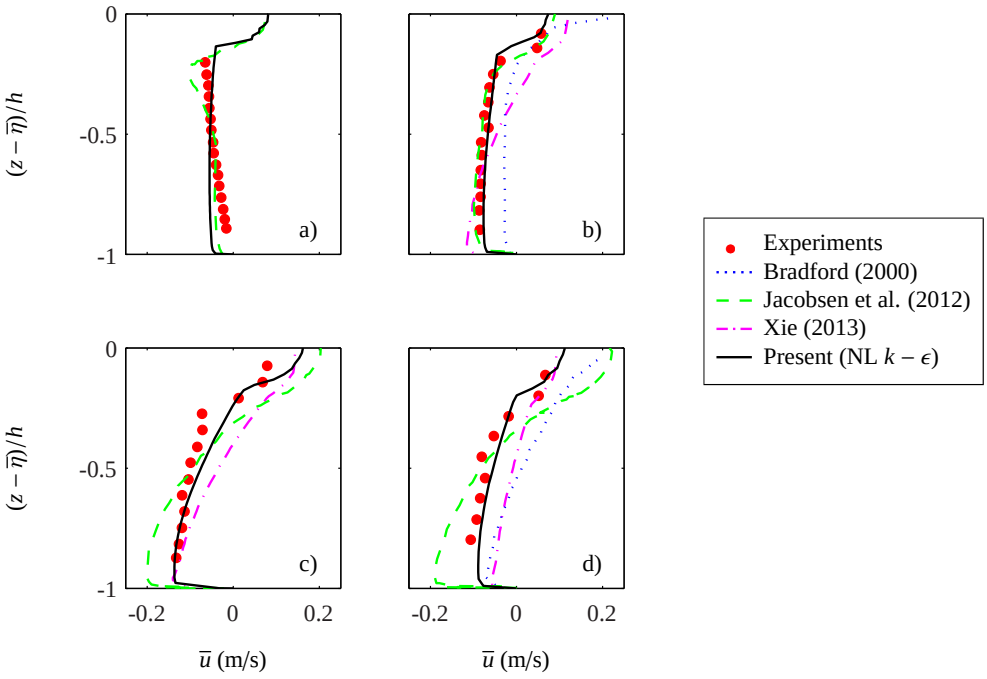

Figure 9: Comparison of time averaged velocity profiles with depth at sampling locations $x - x_b$ = a) -0.455, b) 0.875, c) 2.095 and d) 3.325m. The current model as well as previous numerical models are indicated by the different lines and the dots represent the experimental data collected by Ting and Kirby (1994).

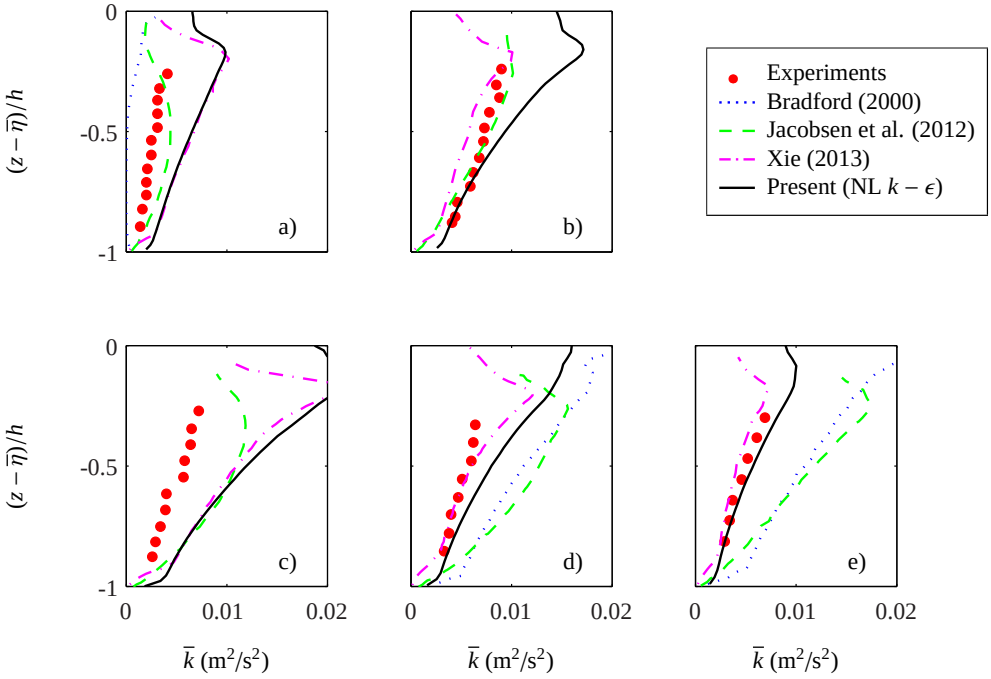

Figure 10: Comparison of time averaged TKE profiles with depth at sampling locations $x - x_b$ = a) 0.875, b) 1.485, c) 2.095, d) 2.71 and e) 3.325m. The current model as well as previous numerical models are indicated by the lines, whereas the dots represent the experimental data obtained by Ting and Kirby (1994).

Table 4. Normalised root mean square error (NRMSE) with respect to the experimental data presented by Ting and Kirby (1994), for both the current and previous numerical models. The model with the lowest NRMSE is indicated by bold text in each case.

		Bradford (2000)	Jacobsen et al. (2012)	Xie (2013)	Current (NL $k-\epsilon$)
η	Max	1.5619	0.0883	0.0880	**0.0868**
	Min	2.3137	0.1194	0.0920	**0.0715**
	MWL	1.2663	-	0.1503	**0.1459**
	Mean	1.7140	0.1039	0.1101	**0.1014**
$\overline{u}$	plot a	-	**0.3797**	-	0.4006
	plot b	0.3291	**0.0802**	0.3207	0.1343
	plot c	-	0.3123	0.3034	**0.1415**
	plot d	0.3410	0.3883	0.3217	**0.1379**
	Mean	0.3351	0.2901	0.3153	**0.2036**
$\overline{k}$	plot a	0.9038	**0.4894**	1.3691	1.3277
	plot b	-	**0.1847**	0.3039	0.5548
	plot c	-	**0.9936**	1.2198	1.4077
	plot d	1.8299	2.0313	**0.3611**	0.7838
	plot e	1.0690	1.6369	0.1865	**0.1823**
	Mean	1.2676	1.0672	**0.6881**	0.8513
Mean		1.2018	0.6095	**0.4288**	0.4479

with the best model shown in bold for each case. Along with an overall mean NRMSE, the mean error for surface elevation, time averaged velocity and time averaged TKE profiles are shown in Table 4. The largest errors in every model, except the one from Bradford (2000), occur in the TKE predictions and the lowest in the surface elevation predictions. Furthermore, it is clear that the nonlinear $k-\epsilon$ in the current study performs better than the previous authors models in terms of surface elevation and velocity profiles, but does not perform as well as Xie (2013) for TKE predictions. The $k-\omega$ model considered earlier in the study (Table 3) shows a similar pattern to the $k-\omega$ model used in Jacobsen et al. (2012), except that the error in the TKE seems to be smaller in the current study.

Overall, it seems that the nonlinear $k-\epsilon$ in the current study is similar if not more accurate than the previous numerical models. The strengths of the model are predictions of surface elevation and time averaged velocity, but it is weaker than the $k-\epsilon$ model used by Xie (2013) and $k-\omega$ in the current study in terms of TKE. This weakness is mainly due to the large differences between the model and experiments at sampling locations a and c. However, it is believed that out of the models considered in this study, the nonlinear $k-\epsilon$ is the best compromise for the application of spilling breakers.

CONCLUSION

In this work, four turbulence closure models have been evaluated for their application to spilling breakers using the open source CFD software, OpenFOAM, along with the additional toolbox, waves2Foam. The models were averaged over twenty wave periods and compared to previous experimental and numerical data. The models were evaluated as to their effectiveness in predicting surface elevation as well as time averaged velocity and TKE. It was found that it is important to include density explicitly in the equations for the turbulence closure models, with certain models being much more sensitive to this change than others.

The results imply that the nonlinear $k-\epsilon$ model captures the surface elevation and undertow best out of the models considered but the $k-\omega$ model predicts the TKE levels more accurately. When compared to previous numerical models, it was found that the current model performs to at least the same standard; predictions of surface elevation and velocity were better but the model of Xie (2013) gave more accurate TKE predictions. Although the $k-\omega$ model yielded a slightly smaller overall mean NRMSE than the nonlinear $k-\epsilon$, the latter model is believed to be the better for application to spilling breakers. The reason for this is that the NRMSE is dramatically increased by a single sampling location for the TKE, but performs well everywhere else. However, in the future, the models will also be compared to the plunging breakers data set in order to further assess which model captures the dynamics of surf zone breakers the best.

References

J. A. Battjes. Surf similarity. In *Proceedings of the 14th International Conference on Coastal Engineering*,, pages 466–480, 1974.

S. F. Bradford. Numerical simulation of surf zone dynamics. *J. Waterw. Port. C-ASCE*, 126, 2000.

E. D. Christensen, J. H. Jensen, and S. Mayer. Sediment transport under breaking waves. In *Proceedings of the 27th International Conference on Coastal Engineering*,, volume III, pages 2467–2480, 2000.

C. R. Iribarren and C. Nogales. Protection de ports. In *XVIIth Int. Nav. Congress*,, volume II, pages 31–80, 1949.

N. G. Jacobsen. *A Full Hydro- and Morphodynamic Description of Breaker Bar Development.* PhD thesis, Technical University of Denmark, Department of Mechanical Engineering, 2011. DCAMM Special Report, no. S136.

N. G. Jacobsen, D. R. Fuhrman, and J. Fredsøe. A wave generation toolbox for the open-source CFD library: OpenFoam®. *Int. J. Numer. Meth. Fluids.*, 70:1073–1088, 2012.

P. Lin and P. L. F. Liu. A numerical study of breaking waves in the surf zone. *J. Fluid Mech.*, 359:239–264, 1998.

S. Mayer and P. A. Madsen. Simulation of breaking waves in the surf zone using a navier-stokes solver. *Proceeding to Coastal Engineering Conference*, I:928–941, 2000.

F. R. Menter. Two-equation eddy-viscosity turbulence models for engineering applications. *AIAA Journal*, 32(8):1598–1605, 1994.

OpenFOAM. The open source CFD toolbox, 2014. http://www.openfoam.com/.

T. H. Shih, J. Zhu, and J. L. Lumley. Calculation of wall-bounded complex flows and free shear flows. *Int. J. Numer. Meth. Fl.*, 23:1133–1144, 1996.

C. G. Speziale and S. Thangam. Analysis of an RNG based turbulence model for separated flows. *Int. J. Eng. Sci.*, 30(10):1379–1388, 1992.

F. C. K. Ting and J. T. Kirby. Observation of undertow and turbulence in a laboratory surf zone. *Coastal Eng.*, 24:51–80, 1994.

F. C. K. Ting and J. T. Kirby. Dynamics of surf-zone turbulence in a spilling breaker. *Coastal Eng.*, 27: 131–160, 1996.

H. K. Versteeg and W. Malalasekera. *An Introduction to Computational Fluid Dynamics: The Finite Volume Method*, pages 40–212. Pearson Education Ltd., 1995.

D. C. Wilcox. Reassessment of the scale-determining equation for advance turbulence models. *AIAA Journal*, 26(11):1299–1310, 1988.

D. C. Wilcox. *Turbulence Modeling for CFD*, pages 1–15. DCW Industries, inc., 3rd edition, 2006.

Z. Xie. Two-phase flow modelling of spilling and plunging breaking waves. *Applied Mathematical Modelling*, 37:3698–3713, 2013.

V. Yakhot, S. Thangam, T. B. Gatski, S. A. Orszag, and C. G. Speziale. Development of turbulence models for shear flows by a double expansion technique. *Phys. Fluids A*, 4(7):1510 – 1520, 1992.